arXiv:1707.08970v3 [astro-ph.EP] 30 Aug 2017

STELLAR WINDS AND DUST AVALANCHES IN THE AU MIC DEBRIS DISK

Eugene Chiang[1,2,4] & Jeffrey Fung[1,3,4]
Draft version September 1, 2017

ABSTRACT

We explain the fast-moving, ripple-like features in the edge-on debris disk orbiting the young M dwarf AU Mic. The bright features are clouds of sub-micron dust repelled by the host star's wind. The clouds are produced by avalanches: radial outflows of dust that gain exponentially more mass as they shatter background disk particles in collisional chain reactions. The avalanches are triggered from a region a few AU across—the "avalanche zone"—located on AU Mic's primary "birth" ring, at a true distance of ∼35 AU from the star but at a projected distance more than a factor of 10 smaller: the avalanche zone sits directly along the line of sight to the star, on the side of the ring nearest Earth, launching clouds that disk rotation sends wholly to the southeast, as observed. The avalanche zone marks where the primary ring intersects a secondary ring of debris left by the catastrophic disruption of a progenitor up to Varuna in size, less than tens of thousands of years ago. Only where the rings intersect are particle collisions sufficiently violent to spawn the sub-micron dust needed to seed the avalanches. We show that this picture works quantitatively, reproducing the masses, sizes, and velocities of the observed escaping clouds. The Lorentz force exerted by the wind's magnetic field, whose polarity reverses periodically according to the stellar magnetic cycle, promises to explain the observed vertical undulations. The timescale between avalanches, about 10 yr, might be set by time variability of the wind mass-loss rate or, more speculatively, by some self-regulating limit cycle.

Keywords: stars: individual (AU Microscopii); protoplanetary disks; stars: winds, outflows; zodiacal dust

1. INTRODUCTION

Dust in debris disks originates from collisional cascades. The largest bodies, comprising the top of the cascade, have lifetimes against collisional disruption equal to the system age, tens of Myrs or longer. They grind down into particles micron-sized or smaller at the bottom of the cascade. These tiny particulates are blown out of the system, typically by stellar radiation pressure, on orbital timescales of tens to thousands of years. For a general review of debris disks, see Matthews et al. (2014).

Quasi-steady cascades, in which the rate of mass erosion is constant from top to bottom (e.g., Dohnanyi 1969; Pan & Sari 2005; Wyatt et al. 2011), offer a ready framework for modeling debris disks on the longest of evolutionary timescales (e.g., Wyatt 2008; Löhne et al. 2008; Gáspár et al. 2013). At the same time, there are increasingly many observations demanding that we resolve our theories more finely, both in space and time, and accommodate more stochastic phenomena. Mid-infrared excesses that are unusually strong given the Gyr ages of their host stars are thought to signal recent catastrophic collisions or sudden comet showers (e.g. Song et al. 2005; Beichman et al. 2005; Wyatt et al. 2005; Weinberger et al. 2011; Kennedy & Wyatt 2013). Fast time variability in the infrared, on timescales of months to years, has been interpreted as tracing the immediate aftermath of a giant plume-inducing impact

(Meng et al. 2014; see also, e.g., Kenyon & Bromley 2005; Melis et al. 2012; Kral et al. 2015).

Of all the short-timescale phenomena reported for debris disks, perhaps the most surprising and least understood is the discovery by the SPHERE (Spectro-Polarimetric High-contrast Exoplanet REsearch) team of fast-moving features in the AU Mic edge-on debris disk (Boccaletti et al. 2015). The features appear as intensity variations at projected stellocentric separations of ∼10–50 AU, and are seen only on the southeast ansa of the disk. They travel away from the star at projected speeds comparable to—and for the most distant features exceeding by a factor of ∼2—the system escape velocity. The features also appear undulatory; the ones closest to the star are elevated by an AU or so above the disk midplane (see also Schneider et al. 2014 and Wang et al. 2015).

Taken at face value, the faster-than-escape velocities, and the trend of increasing velocity with increasing stellar separation, suggest that the brightest features are coherent "clouds" of dust accelerated radially away from the star by a force stronger than the star's gravity by a factor on the order of 10 (Sezestre et al. 2017). We will adopt this simple interpretation. The fact that the clouds are seen to only one side of the star, together with the recognition that most of the mass in the underlying disk is concentrated in a "birth ring" of radius ∼35 AU (Augereau & Beust 2006; Strubbe & Chiang 2006), suggests that the clouds are launched from the birth ring—from the side of the ring nearest the observer, so as to appear bright in forward-scattered starlight—at a special azimuthal location lying directly along the observer's line of sight to the star. Then the clouds simply inherit the orbital motion of the birth ring, whose near side must rotate from the northwest to the southeast to send the

email: echiang@astro.berkeley.edu, jeffrey.fung@berkeley.edu
[1] Department of Astronomy, University of California at Berkeley, Campbell Hall, Berkeley, CA 94720-3411
[2] Department of Earth and Planetary Science, University of California at Berkeley, McCone Hall, Berkeley, CA 94720-3411
[3] NASA Sagan Fellow
[4] The author list is in alphabetical order; all authors contributed equally to the intellectual content and to the work load.

clouds to the southeast.

The host star's wind can generate, for sufficiently small grains, the required radially outward force, of magnitude $\beta_{\rm w}$ relative to stellar gravity:

$$\beta_{\rm w} \equiv \frac{3\dot{M}_* v_{\rm wind}}{16\pi G M_* \rho_{\rm p} s}$$

$$\sim 4 \left(\frac{\dot{M}_*}{10^3 \dot{M}_\odot} \right) \left(\frac{v_{\rm wind}}{400\,{\rm km/s}} \right) \left(\frac{0.1\,\mu{\rm m}}{s} \right) \quad (1)$$

where G is the gravitational constant; $M_* = 0.6 M_\odot$ is the stellar mass (Boccaletti et al. 2015); grains are assumed spherical with internal bulk density $\rho_{\rm p} \sim 1$ g/cm^3 and radius s; and $v_{\rm wind}$ and $\dot{M}_*$ are the stellar wind's speed and mass-loss rate, with the latter scaled to the solar mass loss rate $\dot{M}_\odot = 2 \times 10^{-14} M_\odot/{\rm yr}$ (Cohen 2011). Grain porosity in AU Mic (Graham et al. 2007; Shen et al. 2009) may boost $\beta_{\rm w}$ by an extra factor on the order of 2. Augereau & Beust (2006; see also Schüppler et al. 2015) lay out the many reasons why the mass loss rate from this young, active M dwarf is orders of magnitude larger than the solar mass loss rate. See in particular their Figure 11, which attests that $\beta_{\rm w}$ can be as large as $\sim$40 when AU Mic flares.[5]

We propose here an explanation for the escaping clouds in AU Mic. We posit that they are the outcome of dust avalanches: exponential rises in dust production caused by small grains moving on unbound trajectories and shattering bound disk material in their path (Artymowicz 1997; Grigorieva et al. 2007). In an avalanche, sub-micron grains accelerated to high radial speeds (in this case by the powerful stellar wind) collide with larger parent bodies in the birth ring to create still more sub-micron grains; these collisional progeny are themselves brought up to high speed, leading to a collisional chain reaction and exponential amplification of the escaping dust column. We propose that each of the bright, fast-moving features observed by Boccaletti et al. (2015) results from an avalanche, launched from a small region (a few AU in size) in the birth ring lying directly along the line of the sight to the star (see above). Only in this localized region—what we call the "avalanche zone"—are sub-micron grains produced that can seed the avalanche. In our model, the avalanche zone marks where the birth ring is intersected by another structure: a secondary ring, much less massive than the primary, substantially inclined and/or eccentric, and composed of debris from the catastrophic disruption of a planetesimal. Avalanches are triggered at the intersection point of these two rings, where collisions are especially violent.

Most of the rest of this paper is devoted to reproducing the sizes, masses, and velocities of individual escaping clouds using avalanches. Regarding what sets the periodicity of the avalanches, we have less to say. To match the observations, the avalanche period must be the time between cloud ejections, i.e., the projected separation between clouds divided by their projected velocity. An ap-

proximate, characteristic value for the cycle period is

$$t_{\rm cycle} \sim \frac{10\,{\rm AU}}{5\,{\rm km/s}}$$

$$\sim 10\,{\rm yr}\,. \quad (2)$$

We can imagine two mechanisms that can set this period. The first is time variability in the stellar mass loss rate. This proposal is admittedly somewhat ad hoc. Although AU Mic flares dramatically at ultraviolet and X-ray wavelengths (e.g., Robinson et al. 2001; Augereau & Beust 2006 and references therein), these bursts of high-energy radiation last mere minutes, whereas equation (2) indicates that we are interested in modulating stellar activity on timescales of years. It is not clear whether the similarity between our required value for $t_{\rm cycle}$ and the Sun's 11-year period for magnetic field reversals should be regarded as encouraging or irrelevant. An argument in favor of the latter is that the solar wind mass-loss rate $\dot{M}_\odot$ betrays no correlation with solar magnetic cycle (Cohen 2011). On the other hand, the rate of solar coronal mass ejections (CMEs) increases by an order of magnitude from solar minimum (when the CME rate is 0.5/day) to solar maximum (when the rate is 6/day; Gopalswamy et al. 2003). Magnetic activity cycles are just beginning to be photometrically detected for main-sequence stars *en masse* (Reinhold et al. 2017; there are rumors of a weak correlation between magnetic cycle period and stellar rotation period). For pre-main-sequence stars like AU Mic, there seem to be no useful data on magnetic cycles or on the time evolution of their mass loss rates, although the situation may be changing with long-term monitoring by the Las Cumbres Observatory Global Telescope network (LCOGT; Brown et al. 2013).

An alternative idea is that the stellar wind blows strongly (as is demanded by the observations which point to large $\beta_{\rm w}$) but steadily on yr-to-decade timescales, and that the avalanches undergo some kind of self-regulating limit cycle. It takes time for avalanches to clear and for enough material to re-seed them; this time could be identified with $t_{\rm cycle}$. We will briefly attempt to make this identification at the end of this paper, after quantifying some of the avalanche dynamics in §2. We do not, however, provide an actual limit-cycle model; in particular, we do not answer the key question of why avalanches would not simply unfold in a steady fashion if the stellar wind were steady.

Since the idea of a self-regulating cycle is nothing more than a speculation at this point, we will assume throughout this paper that the avalanche period $t_{\rm cycle}$ is set by the period of a variable stellar mass-loss rate. Fortunately, many of the remaining elements of our proposal do not depend on this assumption. We flesh our model out in §2. A summary, including some predictions and a recapitulation of unresolved issues, is given in §3. In this first cut at a theory, we aim throughout for order-of-magnitude accuracy only.

2. MODEL

We present an order-of-magnitude understanding of the escaping clouds in the AU Mic system. We set the stage in §2.1 by estimating individual cloud masses and mass ejection rates: these are the observables which any

---

[5] Strubbe & Chiang (2006) argue against high mass loss rates in AU Mic, relying instead on stellar radiation pressure to blow out grains. However, they idealized the grain cross section to radiation pressure as geometric; this is an overestimate given real-life optical constants (e.g., Figure 1 of Schüppler et al. 2015).

theory must explain. The heart of our paper is in §2.2, where we sketch our picture of dust avalanches, detailing quantitatively the creation of an avalanche zone from an ancient catastrophic collision; the current properties of the zone; and how the zone can give rise to the observed escaping clouds. In §2.3 we briefly consider magnetic levitation of grains in an attempt to explain the observed vertical displacements of the clouds. To illustrate and provide a proof of concept of our ideas, we offer a numerical simulation in §2.4.

2.1. Cloud Mass and Mass Loss Rate

We estimate the mass of a given cloud using feature "B" (Boccaletti et al. 2015) as a fiducial. The V-band surface brightness of cloud B is comparable to that of the local disk, about $B \sim 16 \, \mathrm{mag/arcsec^2} \sim 0.5 \, \mathrm{erg/(cm^2 \, s \, sr)}$ (Krist et al. 2005; Schneider et al. 2014). We take the line-of-sight column density of grains in the cloud to be N; the scattering cross section per grain to be $Q\pi s^2$; the relative power scattered per grain per steradian to be P (normalized such that its integral over all solid angle equals unity); and a to be the true (not projected) distance between the cloud and the star of luminosity $L_* \sim 0.1 L_\odot$. Then

$$B \sim \frac{L_*}{4\pi a^2} NPQ\pi s^2 \,. \tag{3}$$

The cloud mass is

$$M_\mathrm{cloud} \sim \frac{4}{3}\pi \rho_\mathrm{p} s^3 N A \tag{4}$$

where $A \sim 4 \, \mathrm{AU}$ (length) $\times 2 \, \mathrm{AU}$ (height) is the projected area of the cloud. Combining (3) and (4), we have

$$M_\mathrm{cloud} \sim \frac{16\pi \rho_\mathrm{p} BAsa^2}{3QPL_*}$$
$$\sim 4 \times 10^{-7} M_\oplus \left(\frac{s}{0.1\,\mu\mathrm{m}}\right)\left(\frac{0.3}{Q}\right) \times$$
$$\left(\frac{2/4\pi}{P}\right)\left(\frac{a}{35\,\mathrm{AU}}\right)^2 \tag{5}$$

where we have placed the cloud near the birth ring at

$$a \sim 35 \, \mathrm{AU} \tag{6}$$

and allowed for some forward scattering of starlight by assigning P to be the isotropic scattering value $1/4\pi$ multiplied by a factor of 2. We adopt throughout this paper a nominal cloud grain size of

$$s \sim 0.1\,\mu\mathrm{m} \,, \tag{7}$$

small enough for grains to enjoy high acceleration (equation 1) but still large enough to scatter starlight with reasonable efficiency.

The implied mass loss rate from the debris disk—from clouds only[6]—is

$$\dot{M}_\mathrm{cloud} \sim \frac{M_\mathrm{cloud}}{t_\mathrm{cycle}} \sim 4 \times 10^{-8} M_\oplus/\mathrm{yr} \,. \tag{8}$$

[6] Equation (8) accounts only for the mass ejected in clouds (overdensities). There is also the mass ejected in inter-cloud regions, which we will account for in §2.2.7.

This is a large rate: it would take only ~ 0.25 Myr, or $\sim 1\%$ of the stellar age of $t_\mathrm{age} \sim 23$ Myr (Mamajek & Bell 2014), to drain the disk of $\sim 0.01 M_\oplus$, the total disk mass inferred from millimeter-wave observations (Matthews et al. 2015). This calculation suggests that the episodic ejections we are currently observing have not persisted for the system age, but reflect instead a transient phase. We will provide additional support for this idea in §2.2.4 and §2.2.7.

2.2. Avalanche Dynamics

2.2.1. The Azimuth of the Avalanche Zone, Where Clouds are Launched

We consider a β_w-avalanche composed of 0.1 μm grains accelerated radially across the birth ring. The avalanche occurs in a restricted region on the birth ring—the "avalanche zone"—that is fixed in inertial space. In other words, the azimuth of the zone does not rotate at Keplerian speed (the next section 2.2.2 explains why).

Because (i) the birth ring has a radius of $\sim$35 AU while the cloud closest to the star ("A") is located at a projected separation of $\sim$8 AU, and (ii) all moving features are located on the southeast ansa and travel further southeast, we position the azimuth of the avalanche zone practically directly along the line of sight to the star, at a projected stellar separation $\ll$ 8 AU, so that clouds launched from there can be delivered by disk rotation to the southeast. We also locate the avalanche zone on the half of the ring nearest the observer so that the dust clouds it produces appear bright in forward-scattered light.

2.2.2. The Avalanche Zone Lies Where a Secondary Debris Ring Intersects the Birth Ring; Violent Collisions Here Produce Avalanche Seeds

In our model, the avalanche zone is rooted where the birth ring—hereafter the "primary"—intersects a much less massive "secondary" ring composed of debris from a catastrophically disrupted body (we will place an upper bound on its mass in §2.2.4). The node where the rings intersect is stationary in inertial space (aside from an insignificant precession). A similar set-up was considered in generic terms by Jackson et al. (2014); see also the "static" case of Sezestre et al. (2017) (neither of these studies considered avalanches, and the latter focused on matching the velocity profile of AU Mic's escaping clouds, not their sizes and masses). See Figure 1 for a big-picture schematic.

We imagine the secondary ring to have a semimajor axis and therefore an orbital period comparable to that of the primary,

$$t_\mathrm{orb} \sim 300 \, \mathrm{yr} \,, \tag{9}$$

and to be substantially inclined relative to the primary, reflecting the aftermath of a collision between a projectile in the primary ring and a target (the progenitor of the secondary ring) that once moved on an orbit inclined to the primary by $\sim$1 rad. Alternatively, instead of a large mutual inclination, we could just as well posit a large eccentricity for the secondary progenitor. The secondary ring could then be nearly co-planar with the primary, and be so eccentric that it intersects the primary at the same special azimuthal location of the avalanche zone. The only real requirement on the relative ring geometry is
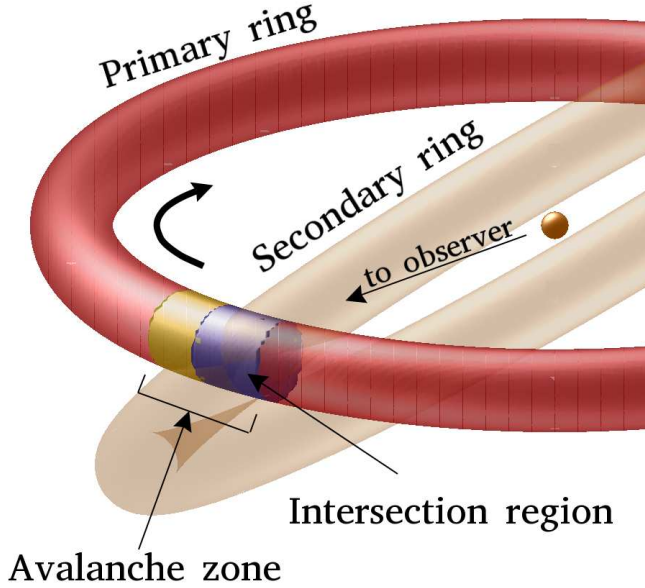
Figure 1. Schematic of our model for AU Mic. The primary (a.k.a. "birth") ring (red) is pierced by a secondary ring (translucent) at the "intersection region" (blue) where primary and secondary ring particles smash into each other at velocities fast enough to generate small 0.1-μm grains. These grains are accelerated radially by the stellar wind to km/s speeds, driving collisional chain reactions with primary ring particles in the "avalanche zone" (blue + yellow). The avalanche zone includes the intersection region and can extend slightly further if seeds have time to travel azimuthally before the stellar wind flushes them out of the system altogether (the direction of primary ring rotation is indicated by the curved arrow). The fast-moving bright features observed by Boccaletti et al. (2015) are clouds of dust launched from the avalanche zone. The ray from the star to the intersection region/avalanche zone points to Earth. The secondary ring is composed of debris from the catastrophic disruption of a planetesimal less than a few hundred km in size. Although we have drawn the secondary ring inclined relative to the primary, it need not be; an eccentric secondary ring is also possible, so long as it creates an intersection region spanning just a few AU.

that this "intersection region" be just a few AU large, in order to match the observed sizes of the escaping clouds (we elaborate on these considerations of size in the next section 2.2.3).[7] We note that the asteroid and Kuiper belts, which are solar system analogues of debris disks, contain bodies commonly moving on highly inclined and eccentric orbits. Given either a large inclination or large eccentricity for the secondary ring, the relative velocities between secondary and primary particles in the intersection region are large:

$$v_{\rm sec,pri} \sim v_{\rm K}/2 \sim 2\,{\rm km/s}\,, \tag{10}$$

i.e., within factors of a few of the local Keplerian velocity

$$v_{\rm K} \sim 4\,{\rm km/s}\,. \tag{11}$$

---

[7] We are positing only one intersection region, but there can be either one or two if the rings are coplanar and eccentric, or two if the rings are circular and inclined and have identical radii. There is no particular reason to think there are two intersection regions based on the Boccaletti et al. (2015) observations, which indicate only a single launch site for grains, but we suppose it is possible that clouds launched from a second intersection region, on the side of the primary ring farther from the observer, could go undetected in back-scattered light.

The intersection region is where 0.1-μm "seeds" for the avalanche are generated from catastrophic collisions between primary and secondary ring particles. The large relative velocities in the intersection region, which approach if not exceed the elastic wave speed in solid rock, readily lead to shattering of primary and secondary ring particles down to the small, $\sim$0.1-μm sizes suitable for strong radial acceleration by the stellar wind (equation 1). We quantify these statements further in §2.2.5.

Outside the intersection region, in the rest of the primary ring, particle relative velocities are too low to generate sub-micron seeds. In the bulk of the primary, which is composed of bound and more nearly micron-sized particles (those dominating the primary's optical depth), relative velocities are of order

$$v_{\rm pri,pri} \sim 100\,{\rm m/s} \tag{12}$$

as judged from the observed vertical thickness of the ring (Strubbe & Chiang 2006). Collisions at such velocities will chip and erode, but do not lead to catastrophic disruption, as they correspond to specific kinetic energies

$$\frac{1}{2}v_{\rm pri,pri}^2 \sim 5 \times 10^7\,{\rm erg/g} \tag{13}$$

that fall short of

$$S^* \sim 2 \times 10^8\,{\rm erg/g} \tag{14}$$

the threshold for catastrophic disruption of micron-sized, relatively flaw-free targets (Grigorieva et al. 2007; Tielens et al. 1994). Thus in non-intersection regions, collisional cascades are not expected to proceed past particle sizes for which $\beta_{\rm w} \sim 0.5$, the minimum threshold for unbinding particle orbits. By contrast, the violence of collisions in the intersection region (equation 10) permits the creation of especially small grains attaining $\beta_{\rm w} \gg 1$.[8]

2.2.3. Sizes of the Intersection Region and of the Avalanche Zone

By definition, the avalanche zone comprises all regions where $\sim$0.1-μm grains (accelerating projectiles) and primary ring particles (field targets that shatter into more projectiles) co-exist. The avalanche zone includes the intersection region where $\sim$0.1-μm seeds are created from collisions between primary and secondary ring particles. Avalanches can also extend beyond the intersection region because seeds can travel azimuthally (at the Keplerian speeds which they inherit at birth from their primary parents), out of the intersection region into the rest of the primary ring. Thus the characteristic dimensions of the avalanche zone and of the intersection region obey (see Figure 1):

$$\Delta l_{\rm avalanche} > \Delta l_{\rm intersect}\,. \tag{15}$$

The size of the intersection region scales with the thickness of the secondary ring (really, a torus); that thickness, in turn, scales with the ejecta velocities $v_{\rm ej}$ of the catastrophic collision that gave birth to the secondary ring:

$$\Delta l_{\rm sec} \sim \frac{v_{\rm ej}}{v_{\rm K}} a \sim 4 \left(\frac{v_{\rm ej}}{400\,{\rm m/s}} \right) {\rm AU} \tag{16}$$

---

[8] At the risk of belaboring the point, an analogy would be with high-energy collisions in a particle accelerator; the greater the energy of the collision, the smaller the constituent particles that are unleashed. See also Leinhardt & Stewart (2012).

(the thickness scales with the dispersion of orbital elements of the secondary fragments, and that dispersion scales with the deviation of fragment orbital velocities from the progenitor's Keplerian velocity). Ejecta velocities $v_{\rm ej}$ of $\sim$200–400 m/s are realistic; see, e.g., modeling of the Haumea collisional family in the Kuiper belt (Lykawka et al. 2012). Our nominal estimate for $\Delta l_{\rm sec}$ is comparable to the radial (Δa) and vertical (H) thicknesses of the primary ring, each of which is about 3 AU (Strubbe & Chiang 2006; Augereau & Beust 2006). The intersection region between secondary and primary rings should be about $\Delta l_{\rm sec}$ large (lower if the originating collision occurred toward the margin of the primary, and higher if the inclination and/or eccentricity of the secondary ring are smaller; see section 2.2.2):

$$\Delta l_{\rm intersect} \sim \Delta l_{\rm sec}\,. \tag{17}$$

An upper limit on $\Delta l_{\rm avalanche}$ is given by the distance that seeds travel azimuthally through the primary ring between avalanches (since a given avalanche triggered during the high phase of the stellar wind flushes the primary of all seeds):

$$\Delta l_{\rm avalanche} < v_{\rm K}\, t_{\rm cycle}$$
$$< 8\,{\rm AU}\,. \tag{18}$$

The actual length $\Delta l_{\rm avalanche}$ will be smaller than this because before seeds have had a chance to cover an azimuthal distance of 8 AU, the stellar wind (during its high phase) will have blown them radially out of the primary.

Equations (15)–(18) constrain $\Delta l_{\rm avalanche}$ to be several AU. This is the right order of magnitude: Boccaletti et al. (2015) observe that the bright fast-moving features are $\Delta l_{\rm cloud} \sim 4$ AU in length. Computing $\Delta l_{\rm cloud}$ from first principles, starting from the considerations outlined here, requires that we fold in the detailed time history of the stellar wind and of the resultant avalanches—this is what we do in the numerical model of §2.4, where we will find that, because of strong radial outflows and projection effects, the intersection region practically single-handedly determines the observed cloud size (i.e., $\Delta l_{\rm cloud} \sim \Delta l_{\rm avalanche} \sim \Delta l_{\rm intersect}$).

Our main takeaway point for this subsection is that, putting aside the various order-unity details, a secondary ring of debris created from a catastrophic collision has the right thickness, namely a few AU (equation 16), to be relevant for the observations by Boccaletti et al. (2015).

2.2.4. The Secondary Ring: Lifetime and Upper Mass Limit

The ejecta velocities of the originating collision place an upper limit on the surface escape velocity of the progenitor: $v_{\rm ej} \sim 400$ m/s implies a progenitor radius $\lesssim 400\,{\rm km}$ or equivalently a progenitor mass

$$M_{\rm sec} \lesssim 10^{-4} M_\oplus \tag{19}$$

where we have assumed a progenitor bulk density of $\sim$2 g/cm^3 (only for equation 19; elsewhere, for less compressed grains, we adopt $\rho_{\rm p} \sim 1$ g/cm^3). A progenitor radius of $\sim$400 km is comparable to those of large asteroids (e.g., Vesta) and Kuiper belt objects (e.g., Varuna).

The secondary ring has a finite lifespan because its particles are destroyed by collisions with the primary ring.

Every time a secondary ring particle executes an orbit, it has a probability of colliding with a primary particle equal to $\tau_{\rm pri}$, the optical depth traversed through the primary ring. That optical depth is on the order of

$$\tau_{\rm pri} \sim 0.01 \tag{20}$$

based on detailed models derived from scattered light images (Augereau & Beust 2006; Strubbe & Chiang 2006). Then the secondary ring disintegrates on a timescale

$$t_{\rm sec} \sim t_{\rm orb}/\tau_{\rm pri}$$
$$\sim 3 \times 10^4\,{\rm yr} \left(\frac{0.01}{\tau_{\rm pri}}\right)\,. \tag{21}$$

By "disintegrate" we refer only to those secondary ring particles small enough to be shattered by the μm-sized particles comprising the bulk of the primary's optical depth. Such secondary ring particles are likely to have sizes smaller than several microns. Despite their restriction in size, such particles may still carry a fair fraction of the mass of the secondary progenitor, for two reasons. The first is that in the immediate aftermath of the progenitor's destruction, ejecta mass is expected to be distributed equitably across logarithmic intervals in fragment size. This expectation arises from the "crushing" law for catastrophic single collisions (Takasawa et al. 2011; Leinhardt & Stewart 2012; Kral et al. 2015).[9] Second, as secondary ring bodies collide with one another and establish an equilibrium cascade, particles near the bottom of the cascade—i.e., μm-sized particles on marginally bound orbits—grow enormously in population because they spend much of their time at the apastra of orbits made highly eccentric by the stellar wind, away from destructive collisions in the secondary ring (see Figure 3 of Strubbe & Chiang 2006). Thus our estimate of the total secondary ring mass $M_{\rm sec}$ may not be that much greater than the mass in μm-sized secondary ring particles; we will assume in what follows that they are within an order of magnitude of one another.

Qualified to refer only to secondary particles small enough to be susceptible to disruption, the lifetime of the secondary ring $t_{\rm sec}$ (which notably does not depend on the secondary ring mass) is some three orders of magnitude shorter than the system age. This aligns with our earlier suspicion (§2.1) that the phenomenon of escaping dust seen today is transient. In fact, the avalanches may not even last as long as $t_{\rm sec}$—see §2.2.7 for the reason why.

2.2.5. Seed Mass and Avalanche Mass

Within the intersection region, primary and secondary ring particles destroy each other to produce 0.1-μm avalanche seeds at a rate

$$\dot{M}_{\rm seed} \sim \frac{M_{\rm sec}}{t_{\rm sec}}\,. \tag{22}$$

---

[9] The crushing law should not be confused with the better known (and often abused) equilibrium cascade describing the long-term comminution of bodies as derived by Dohnanyi (1969; see also Pan & Sari 2005). The latter does not distribute mass logarithmically evenly, but concentrates it in the largest fragments; its use is not appropriate for either short-timescale, non-equilibrium dynamics, or for particle sizes close to the blow-out limit (Strubbe & Chiang 2006).

A couple of comments regarding this estimate: first, although (22) appears superficially to account only for the destruction of secondary ring particles, it actually accounts for the destruction of primary ring particles as well, by symmetry ($\dot{M}_{\rm seed} \sim M_{\rm sec}/t_{\rm sec} \propto M_{\rm sec}\tau_{\rm pri} \propto M_{\rm sec}M_{\rm pri}$, where $M_{\rm pri} \sim 0.01M_\oplus$ is the primary ring mass). Second, underlying statement (22) is the assumption that when primary and secondary ring particles shatter each other, they invest an order-unity fraction of their mass into 0.1-μm grains. Here again we appeal to the crushing law for catastrophic single collisions, which tends to distribute mass logarithmically uniformly across particle sizes; we are not appealing to any equilibrium cascade law like Dohnanyi's (see the discussion in the penultimate paragraph of section 2.2.4).

The 0.1-μm avalanche seeds are accelerated radially outward by the stellar wind over some fraction of $t_{\rm cycle}$. If the "high" phase of the stellar wind lasts

$$t_{\rm high} \sim t_{\rm cycle}/4 \tag{23}$$

then the seeds attain a radial velocity

$$v_\beta \sim \frac{\beta_{\rm w,high}GM_*}{a^2}t_{\rm high}$$
$$\sim v_{\rm K} \left(\frac{\beta_{\rm w,high}}{20}\right)\left(\frac{t_{\rm high}}{t_{\rm cycle}/4}\right). \tag{24}$$

Other values for $t_{\rm high}$ and $\beta_{\rm w,high}$ are possible; only their product matters in (24). (Of course, the product cannot be so high that the larger bodies comprising the primary and secondary rings also become unbound.)

The 0.1-μm seeds slam into more typically μm-sized primary parent bodies, creating more 0.1-μm grains in an exponentially amplifying avalanche. By the time the avalanche has propagated across the radial width of the primary ring, it has traversed an optical depth $\tau_{\rm pri}$ and acquired a mass

$$M_{\rm avalanche} \sim M_{\rm seed}\exp(\eta\tau_{\rm pri}) \tag{25}$$

(see, e.g., the order-of-magnitude description of avalanches by Grigorieva et al. 2007). Here η is the number of fragments produced per catastrophic collision:

$$\eta \sim \frac{(1/2)m_{\rm proj}v_\beta^2}{S^* m_{\rm frag}} \sim \frac{v_\beta^2}{2S^*} \tag{26}$$

where the projectile mass $m_{\rm proj}$ and the individual fragment mass $m_{\rm frag}$ are assumed comparable—both are imagined to correspond to 0.1-μm grains. Inserting (24) into (26) yields

$$\eta \sim 400. \tag{27}$$

An upper limit on η can be estimated by noting that the catastrophic disruption of a 1-μm primary parent particle can yield no more than $\eta_{\rm max} = 1000$ fragments each of size 0.1 μm.

The seed mass underlying a given cloud is that generated during the high phase of the stellar wind (seeds generated during the low phase give rise to the inter-cloud emission; see section 2.2.7):

$$M_{\rm seed} \sim \dot{M}_{\rm seed} \times t_{\rm high}$$
$$\sim 10^{-8}M_\oplus \left(\frac{M_{\rm sec}}{10^{-4}M_\oplus}\right)\left(\frac{\tau_{\rm pri}}{0.01}\right)\left(\frac{t_{\rm high}}{t_{\rm cycle}/4}\right). \tag{28}$$

Putting (25), (27), and (28) together, we derive a single-avalanche mass of

$$M_{\rm avalanche} \sim 5 \times 10^{-7}M_\oplus \left[\frac{\exp(\eta\tau_{\rm pri})}{50}\right]\left(\frac{M_{\rm sec}}{10^{-4}M_\oplus}\right) \tag{29}$$

which is a remarkably good match to the observationally inferred cloud mass $M_{\rm cloud} \sim 4 \times 10^{-7}M_\oplus$ (equation 5), considering that we have not fine-tuned any of the input parameters.

Of course, uncertainties in η and $\tau_{\rm pri}$ will be exponentially amplified in the avalanche gain factor $\exp(\eta\tau_{\rm pri})$. Increasing the gain factor would require that we reduce the secondary ring mass $M_{\rm sec}$ to maintain the agreement between $M_{\rm avalanche}$ and $M_{\rm cloud}$. Thus we can do no better than re-state our upper bound of $M_{\rm sec} \lesssim 10^{-4}M_\oplus$ (equation 19), which in turn implies that avalanche gain factors $\exp(\eta\tau_{\rm pri}) \gtrsim 50$.

Although equation (25) oversimplifies the avalanche dynamics (among other errors, it neglects the finite acceleration times and differing velocities of grains), our conclusions do not depend on the specific implementation of a simple exponential to describe avalanches. Stripped to its essentials, our reasoning can be recapitulated as follows: the mass of an individual cloud is $M_{\rm cloud} \sim 4 \times 10^{-7}M_\oplus$ by equation (5); generically, the mass unleashed in an avalanche is $M_{\rm avalanche} \sim M_{\rm seed} \times$ Gain, where Gain > 1 need not take the form of a simple exponential; $M_{\rm seed} \lesssim 10^{-8}M_\oplus$ by equations (28) and (19); then for $M_{\rm avalanche}$ to match $M_{\rm cloud}$, we need Gain $\gtrsim 40$. Numerical simulations of avalanches by Q. Kral & P. Thébault (personal communication 2017; see also Grigorieva et al. 2007) indicate that such gain factors are possible, even though they are not described by the simplistic exponential in equation (25).

2.2.6. Avalanche Propagation Time

The timescale for the avalanche to propagate radially across the zone (whose size is comparable to the radial width of the primary ring; see §2.2.3) is

$$t_{\rm rad,esc} \sim \Delta l_{\rm avalanche}/v_\beta$$
$$\sim 5\,{\rm yr}\left(\frac{\Delta l_{\rm avalanche}}{4\,{\rm AU}}\right)\left(\frac{20}{\beta_{\rm w,high}}\right) \tag{30}$$

which is both shorter than $t_{\rm cycle} \sim 10$ yr, implying that only one avalanche occurs per stellar cycle, and also longer than our assumed acceleration time of $t_{\rm cycle}/4 \sim 2.5$ yr, as required for consistency.

2.2.7. Total Mass Budget: Cloud + Inter-Cloud Regions, and Starving the Avalanche

That we can reproduce the observed $M_{\rm cloud}$ (equation 5) using our theory for $M_{\rm avalanche}$ (equation 29) is encouraging to us. The theory relies on a variety of estimates,

several of which were made *a priori*, and it is heartening that the numbers hang together as well as they do.

Here is another check on our work. Suppose (just for the sake of making this check; we will see at the end of this subsection why this supposition is probably not realistic) that avalanches continue for the entire lifetime of the secondary ring at their current pace and magnitude. Then the total mass lost from the system should equal the mass of the secondary ring multiplied by the avalanche gain factor:

$$\max M_{\text{total},1} \sim M_{\text{sec}} \exp(\eta\tau_{\text{pri}}) \sim 0.005 M_{\oplus} \,. \quad (31)$$

(See the caveats regarding our use of M_{sec} in section 2.2.4.) We want to check whether this (maximum) mass matches that inferred more directly from observations of mass loss (i.e., Boccaletti et al. 2015). To make this accounting complete, we must include not only the mass lost in clouds ($\dot{M}_{\text{cloud}}$ from equation 8, multiplied by the secondary ring lifetime t_{sec} from equation 21) but also the mass lost from inter-cloud regions. We appeal to our model to account for the latter. The inter-cloud regions represent avalanches from seeds produced during the "low" phase of the stellar wind. Because the duration of the low phase is much less than the orbital time (a.k.a. the system dynamical time), these seeds are not accelerated much beyond their Keplerian speeds during the low phase, and so they stay roughly within the primary ring during this time. Our numerical simulation in section 2.4 confirms this point—the low-phase seeds are distributed along streams that are longer azimuthally than radially. They do not escape radially until the stellar wind attains its high phase, at which time they undergo their own avalanche. Thus while inter-cloud regions are produced from seeds generated during the low phase lasting an assumed $3t_{\text{cycle}}/4$, and clouds are produced from seeds generated during the high phase lasting $t_{\text{cycle}}/4$, both sets of seeds are amplified by about the same avalanche gain factor, because avalanches only occur when the wind is in its high phase. Since the seed production rate is constant (equation 22), the mass-loss rate from inter-cloud regions must be $3\times$ the mass-loss rate from clouds; the total must be $4\times$ the latter. Hence for our second estimate of the total mass lost from the system, we have

$$\max M_{\text{total},2} \sim 4\dot{M}_{\text{cloud}} t_{\text{sec}} \sim 0.005 M_{\oplus} \,. \quad (32)$$

The match between $\max M_{\text{total},1}$ and $\max M_{\text{total},2}$ is better agreement than we probably deserve.

The maximum total mass lost, $\max M_{\text{total}}$, is still less than what the primary ring contains, $M_{\text{pri}} \sim 0.01 M_{\oplus}$, but only by about a factor of 2. The prospect of losing an order-unity fraction of the total disk mass over a small fraction of the stellar age highlights the destructive power of avalanches. But there is good reason to believe that avalanches will not continue unabated for the full lifespan of the secondary ring. If avalanche targets are strictly those at the bottom of a conventional cascade in the primary ring ($\sim\mu$m-sized particles in our simple model, i.e., those dominating the primary ring's optical depth τ_{pri}), then avalanches could be "starved" if the primary cascade does not supply such small targets at a fast enough rate. The primary cascade rate might only be $M_{\text{pri}}/t_{\text{age}} \sim 0.01 M_{\oplus}/(20\,\text{Myr})$, much lower than the current avalanche mass loss rate $M_{\text{total}}/t_{\text{sec}} \sim$

$0.005 M_{\oplus}/(0.03\,\text{Myr})$. Conceivably avalanches weaken well before t_{sec} elapses as the population of μm-sized targets in the primary ring dwindles. Forecasting the long-term evolution of avalanches is left for future work.

2.3. *Vertical Oscillations Driven by the Magnetized Stellar Wind*

The stellar wind, moving with a radial velocity $v_{\text{wind}}\hat{\boldsymbol{r}}$ and carrying a magnetic field $\boldsymbol{B}$, exerts a Lorentz force on dust grains of charge q and velocity $\boldsymbol{v}$:

$$\boldsymbol{F}_{\text{L}} = \frac{q}{c}\left[(\boldsymbol{v} - v_{\text{wind}}\hat{\boldsymbol{r}}) \times \boldsymbol{B}\right] \quad (33)$$

where c is the speed of light.[10] At the large stellocentric distances of interest to us, well outside the wind's Alfvén point, the magnetic field is tightly wrapped and primarily azimuthal: $\boldsymbol{B} \simeq B_{\phi}\hat{\boldsymbol{\phi}}$ (Weber & Davis 1967). The field strength around AU Mic is unknown, but we expect it to be larger than in the solar system, as AU Mic is a rapidly rotating, strongly convective, active young star—properties that all point to a strong stellar magnetic field. For reference, in the solar system, $B_{\phi} \sim 40\,\mu\text{G}\,(a/\text{AU})^{-1}$ (e.g., Schwenn 2000; Weber & Davis 1967). Thus we expect that for the AU Mic system at $a \sim 35$ AU, $B_{\phi} > 1\,\mu\text{G}$.

Given that the field is dominated by its azimuthal component, and that grain velocities $|\boldsymbol{v}|$ are much smaller than $v_{\text{wind}} \sim 400$ km/s, the Lorentz force is dominated by the term proportional to $-v_{\text{wind}}\hat{\boldsymbol{r}} \times B_{\phi}\hat{\boldsymbol{\phi}} = -v_{\text{wind}}B_{\phi}\hat{\boldsymbol{z}}$. This term is equivalent to a vertical electric field $E_{z}\hat{\boldsymbol{z}} = -(v_{\text{wind}}/c)B_{\phi}\hat{\boldsymbol{z}}$ (the electric field seen by a grain when a magnetic field moves past it). We explore in this subsection how we might use this vertical electric field to generate the cloud vertical offsets observed by Boccaletti et al. (2015). We state at the outset that our Lorentz force model will be found wanting in a few respects when confronted with observations (§2.3.2).

In a simple conception of a stellar magnetic cycle, the magnetic field varies sinusoidally with period $t_{\text{mag}} = 2\pi/\omega_{\text{mag}}$:

$$B_{\phi} = B_{\phi,0}\cos(\omega_{\text{mag}}t) \,. \quad (34)$$

The vertical equation of motion for a grain of mass m reads:

$$\ddot{z} = \frac{qE_{z,0}}{m}\cos(\omega_{\text{mag}}t) \quad (35)$$

$$= \frac{-qv_{\text{wind}}B_{\phi,0}}{mc}\cos(\omega_{\text{mag}}t) \,. \quad (36)$$

The solution for the displacement z is oscillatory with a phase that depends on initial conditions, in particular the phase in the magnetic cycle at which the grain is born. A grain born with $z = \dot{z} = 0$ at $t = 0$ (when the field B_{ϕ} is strongest with magnitude $B_{\phi,0}$) is displaced according to

$$z(t \geq 0) = -\frac{qv_{\text{wind}}B_{\phi,0}}{m\omega_{\text{mag}}^2 c}[1 - \cos(\omega_{\text{mag}}t)] \,; \quad (37)$$

it oscillates vertically on one side of the disk, never crossing the midplane to the other side. At the other extreme,

---

[10] Working in cgs units, in which electric and magnetic fields have the same units, and in which the electrical capacitance of a spherical grain equals its radius s.

a grain born with $z = \dot{z} = 0$ at $t = \pi/\omega_{\mathrm{mag}}$ (when B_ϕ is strongest with the opposite polarity $-B_{\phi,0}$) obeys

$$z(t \geq \pi/\omega_{\mathrm{mag}}) = +\frac{qv_{\mathrm{wind}}B_{\phi,0}}{m\omega_{\mathrm{mag}}^2 c}[1 + \cos(\omega_{\mathrm{mag}}t)] \quad (38)$$

and oscillates on the other side. Intermediate cases cross the midplane.

2.3.1. *Magnitude of Vertical Displacements and Parameter Constraints*

The maximum vertical displacement is given by

$$
\begin{aligned}
z_{\mathrm{max}} &= \left| \frac{(q/m)B_{\phi,0}v_{\mathrm{wind}}t_{\mathrm{mag}}^2}{2\pi^2 c} \right| \\
&= 2\,\mathrm{AU} \left(\frac{v_{\mathrm{wind}}}{400\,\mathrm{km/s}} \right) \left(\frac{q/m}{5\times10^{-8}e/m_{\mathrm{p}}} \right) \times \\
&\quad \left(\frac{B_{\phi,0}}{30\,\mu\mathrm{G}} \right) \left(\frac{t_{\mathrm{mag}}}{\mathrm{yr}} \right)^2
\end{aligned}
\quad (39)
$$

where the charge-to-mass ratio q/m is scaled to the proton value e/m_{p}, and we have chosen all input parameters to yield a vertical offset z_{max} similar to that observed for feature "A" by Boccaletti et al. (2015). We can relate q/m to the grain surface potential Φ:

$$
\begin{aligned}
\frac{q}{m} &= \frac{s\Phi}{4\pi\rho_{\mathrm{p}}s^3/3} \\
&\sim 5\times10^{-8}\frac{e}{m_{\mathrm{p}}} \left(\frac{\Phi}{2\,\mathrm{volt}} \right) \left(\frac{0.1\,\mu\mathrm{m}}{s} \right)^2 .
\end{aligned}
\quad (40)
$$

Grains are charged positively by ultraviolet (UV) photoelectric emission; the grain charge equilibrates when the rate at which photoelectrons are ejected (a process that becomes less efficient as the grain increases its positive charge) balances the rate at which ambient stellar wind electrons are absorbed. A surface potential of 2 volts (SI units; equivalent to 2/300 statvolts in cgs) would be comparable to potentials for solar system grains (Kimura & Mann 1998), and would suggest that when scaling from the solar system to AU Mic, the increased number of electrons from the stronger stellar wind nearly balances the heightened UV radiation field. A first-principles calculation of q/m is reserved for future work.

Grains are "picked up" by the magnetized wind to reach stellar wind velocities if they are allowed to complete a magnetic gyration. Since the features are observed to move with velocities much less than v_{wind}, pickup must not have occurred (or at least not fully developed; cf. §2.4). This constrains

$$
\begin{aligned}
1 &> \omega_{\mathrm{gyro}}t_{\mathrm{mag}} \\
&> \frac{qB_{\phi,0}}{mc}t_{\mathrm{mag}}
\end{aligned}
\quad (41)
$$

which re-written in terms of (39) states that

$$\frac{2\pi^2 z_{\mathrm{max}}}{v_{\mathrm{wind}}t_{\mathrm{mag}}} < 1$$

$$0.5 \left(\frac{z_{\mathrm{max}}}{2\,\mathrm{AU}} \right) \left(\frac{400\,\mathrm{km/s}}{v_{\mathrm{wind}}} \right) \left(\frac{\mathrm{yr}}{t_{\mathrm{mag}}} \right) < 1 \quad (42)$$

implying $t_{\mathrm{mag}} > 1$ yr.

2.3.2. *Unresolved Issues with Vertical Deflections*

While our little Lorentz force model predicts an oscillatory vertical motion that recalls the "wavy" structure seen in images of AU Mic (Boccaletti et al. 2015; Schneider et al. 2014), the details of this model do not fit the observations. A key unknown is the period of the magnetic cycle, t_{mag}. One hypothesis sets $t_{\mathrm{mag}} = 2t_{\mathrm{cycle}} = 20$ yr, in the belief that if the stellar mass-loss rate varies with time—which it would do with period t_{cycle} by definition—then it would peak twice per magnetic cycle. In other words, it is imagined that dust avalanches are launched at $t = n\pi/\omega_{\mathrm{mag}}$ for integer n, when the stellar field is strongest irrespective of polarity. The hypothesis that $t_{\mathrm{mag}} \sim 20$ yr runs into the immediate difficulty that the images of AU Mic, spaced in time by significant fractions of t_{mag} (they were taken in July 2010, August 2011, and August 2014) betray no vertical motion for features A and B; these clouds appear to float at a practically constant height of ~ 2 AU above the midplane at three separate epochs.

Faced with this phasing problem, we might hypothesize instead that $t_{\mathrm{mag}} \sim 1$ yr, i.e., the observations just happen to catch the clouds at the same phase. A magnetic cycle period as short as ~ 1 yr marginally satisfies (42). It is not obviously compatible with a stellar-mass cycle period as long as ~ 10 yr (but then again, the stellar-mass loss rate might not vary with this period in the first place; see §1 and §3).

Other mysteries include the observed lack of moving features below the midplane, and the observation that the vertical offsets appear smaller for the most distant clouds. The expected $1/a$ decay in the azimuthal magnetic field strength helps to explain this drop off, but might not be sufficient.

These problems notwithstanding, Lorentz forces still appear the most natural way of explaining the observed vertical undulations. There is no doubt that the stellar wind is magnetized, emanating as it does from a low-mass star, just as there is no doubt that sub-micron grains are charged, bathed as they are in a relatively intense stellar ultraviolet radiation field. Moreover, the sign of the field must periodically reverse, because if it did not, the magnetized wind would eventually pick up grains and accelerate them to speeds and heights far exceeding those observed. What we seem to be missing is an understanding of the detailed time history of the field, and how it is phased with the avalanche history.

2.4. *Numerical Simulations*

We construct numerical simulations to illustrate our ideas, omitting magnetic fields for simplicity. We simulate particles that represent packets of 0.1-μm grains produced in the intersection region and amplified by avalanches. In cylindrical coordinates centered on the star, the particle equations of motion read:

$$\ddot{r} = -\frac{GM_*(1-\beta_{\mathrm{w}})}{(r^2+z^2)^{3/2}}r + \frac{l^2}{r^3} \quad (43)$$

$$\ddot{z} = -\frac{GM_*(1-\beta_{\mathrm{w}})}{(r^2+z^2)^{3/2}}z, \quad (44)$$

where $M_* = 0.6 M_\odot$ and $l = r^2 \dot{\phi}$ is the specific angular momentum, conserved because there are no azimuthal forces (torques). The force ratio $\beta_{\rm w}$ cycles in a step-function manner between a high value $\beta_{\rm w,high} = 20(40)$ lasting $t_{\rm high} = t_{\rm cycle}/4 = 2.5$ yr, and a low value $\beta_{\rm w,low} = \beta_{\rm w,high}/10 = 2(4)$ lasting $t_{\rm low} = 3t_{\rm cycle}/4 = 7.5$ yr. All of the numerical parameters of our simulation are inspired by the various estimates made in §2.2.

The simulation particles are initialized as seeds freshly produced in the intersection region. They begin their trajectories at $r = r_0 = 35$ AU, moving at circular Keplerian speed. Their spatial density in the $\{\phi, z\}$ plane follows a two-dimensional Gaussian representing the intersection region:

$$I_{\phi,z} \propto \exp\left[-\frac{r_0^2(\phi - \phi_0)^2 + z^2}{2\sigma^2}\right], \qquad (45)$$

where ϕ_0 points to the observer. The size of the intersection region is characterized by σ; we choose $\sigma = 1$ AU (the corresponding full width at 2σ is then 4 AU).

We do not explicitly simulate the avalanche process but model it as follows. Each simulation particle is initialized with a fixed baseline mass. When that particle experiences $\beta_{\rm w} = \beta_{\rm w,high}$ for the first time at $t = t_1$, its mass (read: light-scattering cross section) is subsequently amplified by an avalanche gain factor of 50 at $t = t_1 + 5$ yr. The delay time of 5 yr represents the finite propagation time of the avalanche across the primary ring.

We integrate the equations of motion using a second-order leap-frog scheme with a fixed time step of $t_{\rm cycle}/500 = 0.02$ yr. New particles (seeds) are generated in the intersection region at a constant rate of $\sim$15000 particles per year. When constructing surface brightness maps of the disk viewed edge-on, we employ a Henyey-Greenstein scattering phase function with asymmetry parameter $g = 0.25$.

2.4.1. *Simulation Results*

Figure 2 plots the face-on column density of particles from our simulation using $\beta_{\rm w,high} = 20$. The particles trace a zig-zag path as they flow out of the primary ring. The azimuthal segments (zigs) correspond to seeds (+ their subsequent avalanche products) born during the stellar wind's low state: these particles exited the intersection region moving primarily azimuthally. Each initially azimuthal segment was then blown outward when the stellar wind later entered a high state, retaining their azimuthal orientation for subsequent wind cycles (once a zig, always a zig). Conversely, radially oriented segments (zags) contain the seeds (+ their subsequent avalanche products) born during the stellar wind's high state: these particles exited the intersection region moving primarily radially, and remain nearly radial in their orientation as they are blown outward, aside from a small rotational shear (once a zag, always a zag).

Remarkably and encouragingly, Figure 3 shows that the radial segments appear as clouds when viewed edge on. The radial segments have greater line-of-sight column densities than the azimuthal segments do; thus the radial segments appear as bright clouds, while the azimuthal segments represent the inter-cloud regions. We label our brightest clouds A, B, C and D; they seem to compare well with features A through D identified in Fig-
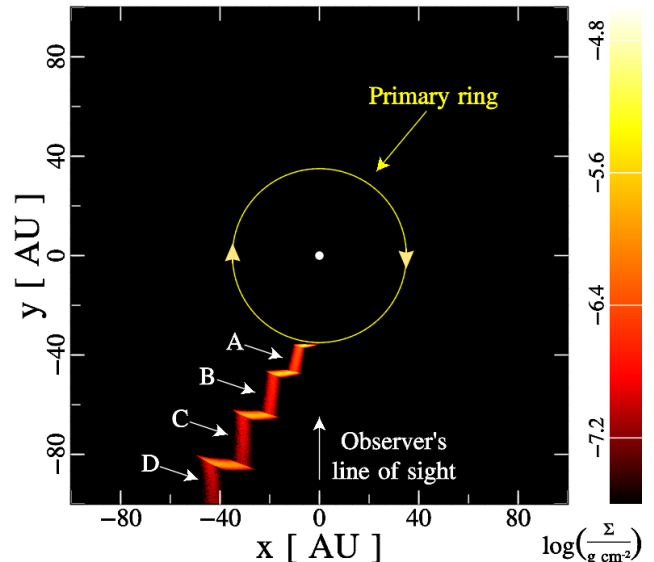

Figure 2. Face-on column density Σ of simulated 0.1-μm grains, launched from the avalanche zone situated on the primary ring, and accelerated outward by a stellar wind whose mass-loss rate varies over a 10-yr period. The primary ring rotates such that its northwest ansa at $x > 0$ approaches the observer and its southeast ansa at $x < 0$ recedes. When the wind is weakest (when $\beta_{\rm w} = \beta_{\rm w,low} = 2$), grains emanate from the primary ring on more nearly azimuthal trajectories; these azimuthal segments retain their orientation as they are blown outward from the star. The radial segments, emerging from the primary ring when the wind blows strongest ($\beta_{\rm w} = \beta_{\rm w,high} = 20$) and here labeled A to D, align with the observer's line of sight; when viewed edge-on (Figure 3), the radial segments have greater projected column densities and appear as bright clouds.

ure 2 of Boccaletti et al. (2015). In particular, the projected separations between our simulated clouds agree with observation.

Projected velocities of the simulation particles, both for $\beta_{\rm w,high} = 20$ and 40, are plotted in Figure 4, together with observational data from Figure 4 of Boccaletti et al. (2015). The agreement is good for observed features A, B, and C, and less good for D and E (note that feature E as identified by Boccaletti et al. 2015 is not a bright cloud but an inter-cloud region). Feature D in particular appears to be something of an outlier, not much helped by increasing $\beta_{\rm w,high}$. To improve the fit, we might look to (*i*) decreasing the launch radius r_0 (thereby increasing our model velocities); (*ii*) incorporating Lorentz forces from the stellar wind (perhaps we are seeing the onset of magnetic pick-up; see the last paragraph of §2.3.1); and (*iii*) independent re-measurement of feature velocities and re-analysis of the uncertainties (see Figure 2 of Sezestre et al. 2017 which reports a new and relatively large error bar on the velocity of feature D.)

3. SUMMARY AND DISCUSSION

We have interpreted the fast-moving features observed in the AU Mic system as coherent clouds of dust produced by periodic avalanches. The clouds are composed of $\sim$0.1-μm grains, small enough to experience a radially outward ram pressure force from the stellar wind up to $\sim$20$\times$ stronger than stellar gravity. The clouds are launched from a region a few AU across—the "avalanche
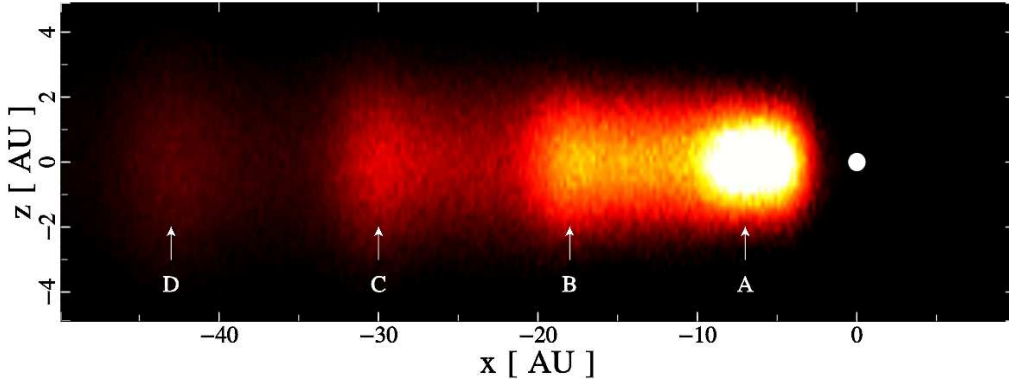
Figure 3. Edge-on view of the same outflowing grains as in Figure 2, here showing scattered-starlight surface brightness instead of raw column density. Cloud A has a surface brightness that is ∼10× higher than cloud D. Compare with Figure 2 of Boccaletti et al. (2015).
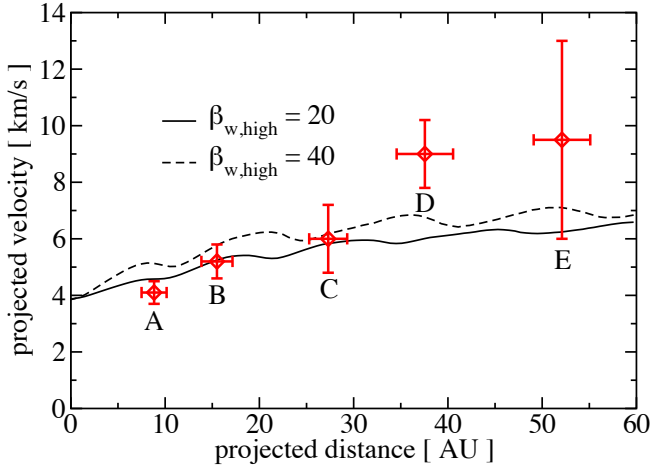

Figure 4. Projected velocity profiles of simulated particles, overplotted with the measured velocities of features A through E from Figure 4 of Boccaletti et al. (2015). Our model agrees well with observation for the inner three features. Some ideas for improving the fit for the outer two features are mentioned in the main text.

zone"—situated on the primary ring encircling the star at ∼35 AU, and lying at an orbital azimuth directly along the line of sight to the star. The avalanche zone marks where a body of radius $\lesssim 400$ km and mass $\lesssim 10^{-4} M_{\oplus}$ was catastrophically disrupted less than ∼3×10^4 yr ago. The debris from that event, now strewn along a secondary ring that intersects the primary ring at the location of the avalanche zone, continues to collide with primary ring particles at km/s speeds, generating the sub-micron grains that seed the avalanche.

This picture can reproduce the individual feature sizes (a few AUs) and masses (∼$4 \times 10^{-7} M_{\oplus}$) inferred from the SPHERE and Hubble Space Telescope observations, using standard collision parameters (e.g., specific energies ∼2×10^8 erg/g for catastrophic disruption of competent targets, and ejecta velocities of a few hundred m/s) and ring parameters validated by previous modeling of the AU Mic disk (e.g., primary ring optical depths on the order of ∼0.01). Avalanche amplification factors exceed $\exp(4) \sim 50$. If avalanches of the kind seen today continue unchecked over the ∼3×10^4 yr lifetime of the secondary ring, then a total mass of ∼$0.005 M_{\oplus}$ would be blown out, roughly half the total mass of the primary ring. In reality, the avalanches may weaken substantially

well before the secondary ring disintegrates, as the number of available targets for disruption (∼μm-sized parents) in the primary ring drops. The rate at which mass is lost through avalanches may eventually asymptote to the rate at which the primary ring erodes mass through a conventional cascade.

Our theory underscores the potential of dust avalanches to transfigure debris disks on timescales much shorter than the age of the star. Dust avalanches leverage the power of chain reactions and exponential amplification to process orders of magnitude more mass than they invest. In our story for AU Mic, avalanches began when a single body less than a few hundred km in size was shattered. That single micro-event opened a "wound" in the parent ring that is now hemorrhaging mass on macro-scales.

The stellar wind is expected to be magnetized, with a field polarity that switches sign according to the stellar magnetic cycle. The resultant oscillating vertical Lorentz force (equivalently, the oscillating vertical electric field seen by grains as the magnetized wind blows past) will alternately lift and lower cloud grains, which are small enough to be significantly charged by stellar ultraviolet photoelectric emission. For plausible input parameters—ambient field strengths on the order of 10s of μG; grain surface potentials on the order of a volt; a magnetic cycle period of a few years—we can reproduce the observed magnitude of the vertical displacements. However, the detailed phasing of the vertical oscillations with time, and their observed decay with increasing projected separation, require further investigation.

We have not specified with confidence the mechanism regulating the avalanche period t_{cycle} (equation 2). We have supposed that it could set by time variability of the host stellar wind. Certainly AU Mic's wind is known to be at least some two orders of magnitude stronger than the solar wind, as judged by the star's flaring activity, and from detailed models of the primary ring which point to significant sculpting by the wind (Augereau & Beust 2006; Schüppler et al. 2015). But to explain how the dust avalanches turn on and off, the wind would need to sustain ∼yr-long gusts every ∼10 yr, causing the star to lose mass at peak rates several thousand times larger than the solar mass loss rate. Whether such extreme and sustained episodes of stellar mass loss are actually realized, and whether we can reconcile the stellar mass-

loss cycle with the stellar magnetic cycle (as traced by the cloud vertical displacements; see above), are outstanding issues.

We wonder whether we might dispense with the need for decadal-timescale variability in the stellar mass-loss rate by positing instead some kind of limit-cycle instability in the avalanche zone. The order-of-magnitude similarity between the required cycle period ($\sim$10 yr) and the time it takes for the avalanche to propagate radially across the parent ring ($\sim$5 yr from equation 30) suggests that perhaps the avalanche zone regulates itself—that avalanches are triggered when some threshold condition is periodically satisfied in the intersection region. It must be some condition on the seed optical depth. Conceivably the avalanche evacuates the zone so thoroughly of seeds that the system needs time to re-fill. Avalanches are characterized by exponential amplification, and with exponentials there is extreme sensitivity to environmental conditions. At the moment we are unable to say more than this, but the possibility of a self-regulating limit cycle (and a stellar wind that is steady but that still needs to blow strongly to achieve the large force ratios $\beta_{\rm w} \sim 10$ implied by the observed cloud velocities) seems deserving of more thought. Note that while distinct clouds are created from line-of-sight projection effects in our time-variable stellar-wind model (§2.4), they would be created instead by time variability in the avalanche dust production rate in the limit-cycle picture.

Regardless of what drives the time variability, the avalanche zone from which dust clouds are launched remains fixed in inertial space. By contrast, orbiting sources of escaping dust (e.g., a planet—putting aside the separate problem of how a planet could be a source of dust in the first place) tend to follow the dust that they eject, since the observed velocities of the features are comparable to orbital velocities at $\sim$35 AU. This similarity of velocities leads to immediate difficulties in using a moving source to reproduce the observed spacing between features; the resultant clouds will be too closely spaced if launched from a moving source near the primary ring at $\sim$35 AU. Our model avoids this problem altogether because the dust launch zone is located at the intersection of two rings; this node does not move, aside from a negligible precession.

Although our proposal contains significant room for improvement, it points to a few observational predictions: (*i*) the escaping cloud grains should have smaller sizes (the better to be accelerated outward, and to be electrically charged) than their counterparts bound to the primary and secondary rings; the size difference could be confirmed by measuring color differences between the fast-moving features and the rest of the disk (a pioneering attempt to spatially resolve color differences has been made using the Hubble Space Telescope by Lomax et al. 2017); (*ii*) assuming there is only a single avalanche zone (i.e., a single intersection point between the primary and secondary rings) located directly along the line of sight to the star, all escaping clouds will always be seen on the southeast ansa of the disk; (*iii*) the primary ring should rotate such that the northwest ansa approaches the Earth while the southeast ansa recedes from it. This sense of rotation is not a crucial detail of our model, but is preferred because it situates the avalanche zone on the side of the primary ring nearest the observer, so that

the clouds launched from there are seen more easily in forward-scattered than in back-scattered starlight. Spectral line observations in CO gas can test our expectation; (*iv*) the secondary ring has a mass $< 1\%$ that of the primary, and might be distinguished from the primary (this is admittedly ambitious) in ultra-deep exposures if the rings are mutually inclined; and (*v*) what goes up should come down: the features should be observed to vary their vertical positions according to the stellar magnetic cycle.

REFERENCES

Artymowicz, P. 1997, Annual Review of Earth and Planetary Sciences, 25, 175
Augereau, J.-C., & Beust, H. 2006, A&A, 455, 987
Beichman, C. A., Bryden, G., Gautier, T. N., et al. 2005, ApJ, 626, 1061
Boccaletti, A., Thalmann, C., Lagrange, A.-M., et al. 2015, Nature, 526, 230
Brown, T. M., Baliber, N., Bianco, F. B., et al. 2013, PASP, 125, 1031
Cohen, O. 2011, MNRAS, 417, 2592
Dohnanyi, J. S. 1969, J. Geophys. Res., 74, 2531
Gáspár, A., Rieke, G. H., & Balog, Z. 2013, ApJ, 768, 25
Gopalswamy, N., Lara, A., Yashiro, S., Nunes, S., & Howard, R. A. 2003, in ESA Special Publication, Vol. 535, Solar Variability as an Input to the Earth's Environment, ed. A. Wilson, 403–414
Graham, J. R., Kalas, P. G., & Matthews, B. C. 2007, ApJ, 654, 595
Grigorieva, A., Artymowicz, P., & Thébault, P. 2007, A&A, 461, 537
Jackson, A. P., Wyatt, M. C., Bonsor, A., & Veras, D. 2014, MNRAS, 440, 3757
Kennedy, G. M., & Wyatt, M. C. 2013, MNRAS, 433, 2334
Kenyon, S. J., & Bromley, B. C. 2005, AJ, 130, 269
Kimura, H., & Mann, I. 1998, ApJ, 499, 454
Kral, Q., Thébault, P., Augereau, J.-C., Boccaletti, A., & Charnoz, S. 2015, A&A, 573, A39
Krist, J. E., Ardila, D. R., Golimowski, D. A., et al. 2005, AJ, 129, 1008
Leinhardt, Z. M., & Stewart, S. T. 2012, ApJ, 745, 79
Löhne, T., Krivov, A. V., & Rodmann, J. 2008, ApJ, 673, 1123
Lomax, J. R., Wisniewski, J. P., Roberge, A., et al. 2017, ArXiv e-prints, arXiv:1705.09291
Lykawka, P. S., Horner, J., Mukai, T., & Nakamura, A. M. 2012, MNRAS, 421, 1331
Mamajek, E. E., & Bell, C. P. M. 2014, MNRAS, 445, 2169
Matthews, B. C., Krivov, A. V., Wyatt, M. C., Bryden, G., & Eiroa, C. 2014, Protostars and Planets VI, 521
Matthews, B. C., Kennedy, G., Sibthorpe, B., et al. 2015, ApJ, 811, 100
Melis, C., Zuckerman, B., Rhee, J. H., et al. 2012, Nature, 487, 74
Meng, H. Y. A., Su, K. Y. L., Rieke, G. H., et al. 2014, Science, 345, 1032
Pan, M., & Sari, R. 2005, Icarus, 173, 342
Reinhold, T., Cameron, R. H., & Gizon, L. 2017, A&A, 603, A52
Robinson, R. D., Linsky, J. L., Woodgate, B. E., & Timothy, J. G. 2001, ApJ, 554, 368

Schneider, G., Grady, C. A., Hines, D. C., et al. 2014, AJ, 148, 59

Schüppler, C., Löhne, T., Krivov, A. V., et al. 2015, A&A, 581, A97

Schwenn, R. 2000, Solar Wind: Global Properties, ed. P. Murdin

Sezestre, É., Augereau, J.-C., Boccaletti, A., & Thébault, P. 2017, ArXiv e-prints, arXiv:1707.09761

Shen, Y., Draine, B. T., & Johnson, E. T. 2009, ApJ, 696, 2126

Song, I., Zuckerman, B., Weinberger, A. J., & Becklin, E. E. 2005, Nature, 436, 363

Strubbe, L. E., & Chiang, E. I. 2006, ApJ, 648, 652

Takasawa, S., Nakamura, A. M., Kadono, T., et al. 2011, ApJ, 733, L39

Tielens, A. G. G. M., McKee, C. F., Seab, C. G., & Hollenbach, D. J. 1994, ApJ, 431, 321

Wang, J. J., Graham, J. R., Pueyo, L., et al. 2015, ApJ, 811, L19

Weber, E. J., & Davis, Jr., L. 1967, ApJ, 148, 217

Weinberger, A. J., Becklin, E. E., Song, I., & Zuckerman, B. 2011, ApJ, 726, 72

Wyatt, M. C. 2008, ARA&A, 46, 339

Wyatt, M. C., Clarke, C. J., & Booth, M. 2011, Celestial Mechanics and Dynamical Astronomy, 111, 1

Wyatt, M. C., Greaves, J. S., Dent, W. R. F., & Coulson, I. M. 2005, ApJ, 620, 492